Journal of Volcanology and Geothermal Research 456 (2024) 108218

Contents lists available at ScienceDirect

Journal of Volcanology and Geothermal Research

journal homepage: www.journals.elsevier.com/journal-of-volcanology-and-geothermal-research

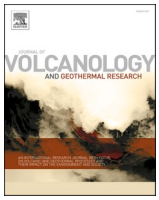

The influence of Fe—Ti oxide microlites on bubble nucleation in rhyolitic melts

Wade L. Aubin [*,1], James E. Gardner

Department of Earth and Planetary Sciences, Jackson School of Geosciences, The University of Texas at Austin, Austin, TX 78712, United States of America

ARTICLE INFO

Keywords:
Heterogenous bubble nucleation
Magnetite
Rhyolitic magma
Supersaturation
Nucleation theory
Explosive eruptions

ABSTRACT

We conducted a set of high-temperature decompression experiments to constrain the mechanisms of heterogeneous bubble nucleation in high-silica rhyolitic melt that contained 4.6–4.8 wt% H_2O. The melt was seeded with two different size fractions of magnetite crystals: 1–2 μm crystals and large crystals of 32–135 μm (long axis). The number density of bubbles (BND) that nucleated on the small crystals was found to increase from $10^{6.5}$ to $10^{8.7}$ cm^{-3} as H_2O increasingly supersaturated (ΔP) in the melt from 3 to 23 MPa. At ΔP >23 MPs, however, the number of bubbles nucleated equals the number of small magnetite and no more nucleated with increased ΔP. At the same conditions, the number of bubbles that nucleated on the large crystals increases, from <1 bubble per crystal at ΔP = 3 MPa to 14 ± 4 bubbles per crystal at 58 MPa. We thus find that ΔP has a significant influence on the mechanisms of heterogenous nucleation, but the observed increases in BND are much greater than would be predicted solely from the increase in ΔP. The discrepancy can be reconciled if there are different sites on the crystals that become activated at greater ΔP, leading to greater numbers of bubbles nucleating. The cumulative BND nucleated on small crystals, however, is capped by the number of crystals present. The BND values generated at ΔP >23 MPa in our experiments overlap with those found in ~80 % of naturally occurring pumice. Assuming our experiments are representative of natural pumice, this suggests that explosively erupted magmas either become significantly volatile supersaturated before heterogeneously nucleating bubbles, or that the number of nucleation sites in natural magmas greatly exceed 10^9 cm^{-3}.

1. Introduction

Explosive volcanic eruptions are driven by the rapid release of gas, mainly H_2O and CO_2, that was dissolved in magma at depth (Sparks, 1978; Proussevitch and Sahagian, 1996, 1998, 2005; Sahagian, 2005; Girona et al., 2016; Tramontano et al., 2017). Magma degasses as it ascends to the surface because the solubilities of H_2O and CO_2 in silicate melt decrease with decreasing pressure (Iacono-Marziano et al., 2012; Iacovino et al., 2013; Liu et al., 2005). Models for the intensity and style of volcanic eruptions thus need to account for mechanisms of magma degassing, the escape of volatile species from the melt. A critical step in the degassing process is the nucleation of gas bubbles, which occurs when clustering of gas molecules in response to supersaturation (ΔP) overcomes thermodynamic barriers and stabilizes a new bubble phase (Hirth et al., 1970; Hurwitz and Navon, 1994; Gardner et al., 2023). Numerous studies have thus focused on bubble nucleation in silicic magmas (e.g., Hurwitz and Navon, 1994; Gardner et al., 1999; Mourtada-Bonnefoi and Laporte, 1999; Mangan and Sisson, 2000; Gardner and Denis, 2004; Mangan et al., 2004; Gardner, 2007, 2012; Iacono-Marziano et al., 2007; Cluzel et al., 2008; Larsen, 2008; Hamada et al., 2010; Cichy et al., 2011; Gardner and Ketcham, 2011; Gardner et al., 2013, 2018a; Gonnermann and Gardner, 2013; Fiege et al., 2014; Gardner and Webster, 2016; Le Gall and Pichavant, 2016; Hajimirza et al., 2019, 2021).

Despite the extensive body of research, there is yet no universal model for predicting the mechanisms and rates of bubble nucleation in magmas (Gardner et al., 2023). A key gap in our knowledge is the kinetics of heterogeneous nucleation, in which gas bubbles nucleate on pre-existing crystals in magma as result of lower surface tension. Previous studies have identified crystal phases that facilitate bubble nucleation to various degrees (e.g. Hurwitz and Navon, 1994; Gardner and Denis, 2004; Larsen, 2008; Shea, 2017; Cáceres et al., 2022). Very little data exist however, to constrain the rates of heterogeneous nucleation and to relate nucleation to sizes or numbers of crystals in

* Corresponding author.
E-mail address: waubin@coloradomesa.edu (W.L. Aubin).
[1] Present Address: Department of Physical and Environmental Sciences, Colorado Mesa University, Grand Junction, CO, 81501, U.S.A.

https://doi.org/10.1016/j.jvolgeores.2024.108218
Received 28 August 2024; Received in revised form 29 October 2024; Accepted 31 October 2024
Available online 8 November 2024

magma (Gardner et al., 2023).

To better constrain the kinetics of heterogenous bubble nucleation, we conducted a series of isothermal experiments using hydrated rhyolite melts that were decompressed over a range of ΔP values. The melts were seeded with different populations of magnetite crystals to serve as nucleation sites. Magnetite is a common accessory mineral in rhyolitic magmas and is known to substantially reduce the ΔP required to nucleate bubbles (Hurwitz and Navon, 1994; Gardner and Denis, 2004). Here, we find that heterogeneous bubble nucleation increases with ΔP, but can be limited by the number density of crystals present, depending on crystal size. Magnetite smaller than ~5 μm can serve as a nucleation site for only one bubble, whereas at a given ΔP more than one bubble can nucleate on larger magnetite crystals.

2. Methods

Starting materials for all experiments consisted of hydrated rhyolitic glass and populations of magnetite crystals. To make the glass, cylinders, ~1.5 cm long and 3 mm in diameter, were cored from high silica rhyolitic obsidian that consists of clear rhyolitic glass and less than 1 vol % microlites (Table 1). Sharp edges of each cylinder were ground with emery cloth to prevent puncturing of the Au tube in which they were hydrated. Each cylinder was inserted into a 4-mm O.D. Au capsule that was welded shut on one end. An amount of distilled water that equaled ~8 wt% of the cylinder was added to the capsule to ensure complete hydration during the experiment. The open end of the capsule was then welded shut, and the sealed capsule was weighed, heated to 110 °C for 10 min, and then reweighed to check that the capsule did not leak. The capsule was then inserted into an externally heated, cold-seal pressure vessel made of a Nickel-based alloy. The pressure vessel was attached to a pressure line, and pressure was applied using water. The vessel was then placed into a horizontal furnace and the sample was hydrated at 850 °C and 100 MPa for 120 h. A thin section was made of a small piece of the hydrated cylinder to check the glass for any residual crystals. The hydrated sample was then ground to powder using a mortar and pestle, and the powder was sieved to <45 μm.

To produce starting materials that contained magnetite, ~100–150 mg of the hydrated glass powder was mixed with ~1 wt% (~0.5 vol%) angular and blocky magnetite crystals that range in size from 32 to 135 μm (long dimension) to 6–45 μm (short dimension). The mixture was loaded into a 4-mm O.D. Au capsule that had been welded shut on one end. The other end of the capsule was left open. The capsule was placed into a sample holder at the end of an Inconel rod, which was then inserted into a pressure vessel made of Nickel-based alloy that was fitted with a rapid quench extension (Gardner, 2007). The pressure vessel was connected to the pressure line, pressure was applied using water, and a furnace was lowered over the pressure vessel. Because the capsule was open, the pressurizing water was in contact with the powder and crystals, ensuring complete H_2O saturation during the experiments (Gardner et al., 2019). An external magnet held the sample in the water-cooled end of the pressure vessel while the vessel was heated. Once the pressure vessel equilibrated thermally, the magnet was raised to lift the sample into the hot zone of the pressure vessel. The sample was sintered at 850 °C and 100 MPa for one hour, during which pressure varied by no more than 0.1 MPa and temperature varied by no more than 2 °C. The furnace was then turned off and the sample cooled isobarically to 500 °C at a rate ~ 8 °C min^{-1} to resorb any bubbles in the glass (Gardner et al., 2019). Upon reaching 500 °C, the sample was quenched by quickly lowering the external magnet, bringing the sample into the water-cooled region of the vessel where it cooled at ~150 °C s^{-1} (Gardner et al., 2018b).

Four separate starting materials were made (Table 2). Thin sections made of three of those revealed that during cooling the glass crystallized <1 vol% blocky magnetite that are <1–5 μm in size and occur in number densities (MND) of $10^{8.8–9.0}$ cm^{-3} (Table 2). Measurements of the glass in those three samples using Fourier Transform Infrared (FTIR) spectroscopy showed that the glass contained 4.6–4.8 wt% H_2O, which is equivalent to saturation at ~133–143 MPa at 850 °C (Liu et al., 2005). The increased H_2O content results from resorption of bubbles during cooling (Gardner et al., 2019). The fourth starting sample was not analyzed before decompressions, but examination of the final products reveal that it also contained the same population of small magnetite. We assume that it had a dissolved H_2O content equal to the average value of the other three samples.

Twelve decompression experiments were carried out using splits from samples of the starting materials described in the previous paragraph (Table 3). Each experiment consisted of 30–50 mg of starting material loaded into 4–mm O.D. Au capsules that had been welded at one end and placed into the same rapid-quench pressure vessel configuration described above. Each was thermally equilibrated for five minutes at 850 °C and 160 MPa, a pressure high enough to ensure that no bubbles nucleated prior to decompression. After five minutes, pressure was decreased nearly instantaneously (~1–2 s) down to 80–150 MPa and held for 30–600 s before quenching (Table 3).

One decompression experiment consisted only of ~50 mg of hydrated rhyolitic powder (Table 3). This experiment was sintered and cooled as described above but was then reheated to 850 °C and 160 MPa for five minutes and then decompressed to 130 MPa and held for 900 s. Inspection of the product shows that the population of small magnetite crystals grew as before, and so we are confident that it differs from the other 12 only in its lack of larger magnetite.

Thin sections were made of each run product, and they were examined using a petrographic microscope to characterize the bubble population that nucleated and the relationship between those bubbles and the two populations of magnetite crystals. Bubble number density (BND) was measured by selecting six different areas, each 60 μm × 60 μm in size, and counting all bubbles on small microlites while focusing through

Table 1
[a,b]Rhyolitic obsidian used in this study.

Oxide	Concentration
SiO_2	76.53
TiO_2	0.06
Al_2O_3	13.01
FeO	0.79
MnO	0.08
MgO	0.02
CaO	0.74
Na_2O	3.87
K_2O	4.91

[a] Major clement composition by electron microprobe, normalized on an anhydrous basis (100 %) with all Fe reported as FeO; oxides are in weight percent.

[b] Composition originally published in Gardner, 2009

Table 2
Starting materials for Decompression Experiments.

	P[1] (MPa)	T_o[2] (°C)	T_f[3] (°C)	$[H_2O]$[4] (wt%)	MND[5] (cm^{-3})
A-132	100	850	500	4.80 ± 0.12	$10^{8.9}$
A-133	100	850	500	4.61 ± 0.13	$10^{8.8}$
A-148	100	850	500	*n.a.*	*n.a.*
A-153	100	850	500	4.68 ± 0.72	$10^{9.0}$

[1] Pressure.

[2] Temperature for sample sintering, held for 60 min.

[3] Final temperature after sample cooled.

[4] Dissolved H_2O contents (in wt%) in glass of starting materials, as measured using FTIR (see Methods); *n.a.* = not analyzed.

[5] Microlite number density (in numbers of crystals per cm^3) of small magnetite microlites grown during cooling from T_o to T_f; *n.a.* = not analyzed.

Table 3
Run conditions and results of decompression experiments.

	Starting[1] material	T[2] (°C)	P_s[3] (MPa)	P_f[3] (MPa)	ΔP[4] (MPa)	time[5] (s)	BND[6] (cm^{-3})	Bubbles[7] On large XL
A-152	A-148	850	160	150	–	150	$10^{5.4}$	<1
A-143	A-133	850	160	150	–	300	$10^{5.1}$	<1
A-151	A-148	850	160	150	–	450	$10^{5.5}$	<1
A-137	A-132	850	160	140	3	300	$10^{6.4\pm0.24}$	5 ± 3
A-154	A-153	850	160	130	6	300	$10^{7.1\pm0.40}$	–
A-155	A-153	850	160	130	6	600	$10^{7.6\pm0.17}$	–
G-1865	–	850	160	130	6	900	$10^{7.1\pm0.40}$	–
A-142	A-133	850	160	120	13	30	$10^{7.2\pm0.22}$	6 ± 3
A-140	A-133	850	160	120	13	150	$10^{8.1\pm0.13}$	9 ± 4
A-141	A-133	850	160	120	13	450	$10^{8.0\pm0.24}$	7 ± 3
A-138	A-132	850	160	120	23	300	$10^{8.1\pm0.34}$	11 ± 7
A-139	A-132	850	160	100	43	300	$10^{8.7\pm0.23}$	13 ± 6
A-149	A-148	850	160	80	58	300	$10^{8.7\pm0.04}$	14 ± 4

[1] Starting material used in experiment (Table 1). Starting material for G-1865 was hydrated glass powder (see methods for details).
[2] Experimental temperature.
[3] P_s = starting pressure (sample held for 5 min at this pressure), P_f final pressure reached in ~1–2 s.
[4] Supersaturation pressure equal to the difference between the saturation pressure calculated from the initial H_2O content of the starting material (~142 MPa) and P_f; It is assumed that glass in G-1865 initially contained 4.8 wt% H_2O, equivalent to 142 MPa; "–"= undersaturated conditions.
[5] time (in seconds) sample was held at P_f before being quenched instantaneously.
[6] Number density of bubbles nucleated on small magnetite crystals, in number of bubbles per cm^3.
[7] Average number of bubbles nucleated on large magnetite crystals.

the sample. Depth was measured using a Heidenhain focus drive linear encoder attached to the focusing drive of the microscope. The average error for depth measurements is ±0.6 μm, based on repeated focusing through a sample (e.g., Gardner et al., 2013). Counting errors were determined by selecting six samples and counting the numbers of bubbles in six different volumes in each sample six different times. We find that the error on BND is ~8 %, resulting mainly from sample heterogeneity. We verified this method by conducting repeated measurements of samples with known values. BND values reported are for the total number of bubbles counted within the entire volume of sample analyzed (Table 3). Bubbles form less than ~5 vol% of the samples, and most often <1 vol%. We thus did not correct BND to melt volume only.

Using an optical microscope, we accurately observed bubbles as small as ~0.5 μm in diameter. In any experiment, regardless of the amount of decompression or the decompression time, the minimum bubble size observed was no smaller than ~1 μm, and the great majority of bubbles were 3–6 μm diameter. If there were bubbles smaller than this, we would expect to see a range of bubble sizes from <0.5 μm–6 μm in diameter. Instead, we see the majority of bubbles clustering around 3–6 μm in diameter.

For the large magnetite crystals, instead of counting BND, we chose 10 large crystals per sample and counted the number of bubbles attached to those crystals. We did this for several reasons. First, BND is a bulk term specifying the number of bubbles that are expected in a given volume of melt. Since the large magnetite crystals are heterogeneously distributed it would be misleading to include bubbles attached to them in a bulk term or to report them using a bulk term. Second, the BND term defines the number of bubbles that are expected to nucleate in any given volume of melt. In the case of the large magnetite crystals, the only melt involved is some unknown volume adjoining the crystal. Because this volume is not definable for the experiments, we cannot calculate the BND. Third, the large magnetite crystals equal ~0.5 vol% in each experiment. Assuming spherical crystals with a diameter of ~50 μm, then the number of crystals equals ~7×10^5 cm^{-3} per sample. If each crystal has 10 bubbles, BND equals 7×10^6 cm^{-3}. Ten bubbles per large magnetite crystal would be expected only at high ΔP, in which BND on the small magnetite microlites is ~1×10^8 cm^{-3}. Adding the number of bubbles on the large crystals to the BND of bubbles on the small microlites equals ~1.01×10^8 cm^{-3}. The difference between the BNDs is smaller than the precision of our measurement, and hence, is not significant. We chose the number 10 because it becomes increasingly difficult to accurately count bubbles on crystals deeper in a sample, especially those with high BND. Therefore we counted bubbles attached to large crystals that were close to the surface of the thin section. We chose crystals that were as close to parallel as possible with the thin section surface and only counted bubbles that were along the sides of

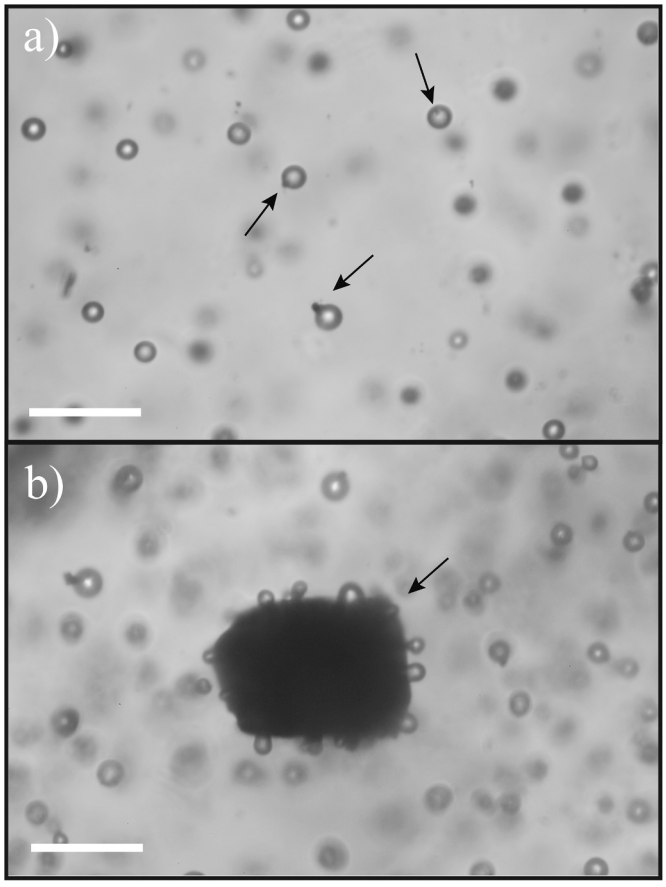

Fig. 1. a) Photomicrograph of experiment A-141 showing single bubbles each attached to small magnetite microlites. b) Experiment A-138 showing multiple bubbles attached to a single large magnetite crystal. White scale bars are 25 μm long.

crystals as viewed in two dimensions (e.g. Fig. 1b).

3. Results

Rhyolite glasses in the starting materials contain 4.6–4.8 wt% H_2O, equivalent to H_2O saturations of 133–143 MPa (Liu et al., 2005). Samples were thus thermally equilibrated at 160 MPa before being decompressed to prevent bubble nucleation. Three samples were decompressed to 150 MPa and held for 150–450 s (Table 3). Very few bubbles exist in those samples, with BND values of $\sim 10^{5.1–5.5}$ cm^{-3}. Those bubbles are most likely ones that were left after sintering and cooling. These samples provide the baseline to establish whether bubbles found in samples decompressed to lower pressures had nucleated at the lower pressures. All samples decompressed below 150 MPa contain a large number of bubbles in their outer 10's of microns. These are most likely "fringe" bubbles that occur almost ubiquitously in decompressions of hydrous melts as a result of heterogeneous nucleation where the melt is in contact with the metal capsule (Mangan and Sisson, 2000; Gardner and Webster, 2016). We ignored these bubbles and focused on those formed in the interiors of samples.

Within the interiors of all samples decompressed below 150 MPa bubbles nucleated in BND values from $10^{6.4}$ to $10^{8.7}$ cm^{-3}, one to three orders of magnitude more bubbles than in the 150 MPa experiments (Table 3). In fact, the number of bubbles found in the 150 MPa experiments could make up only ~0.03–4 % of the total bubble population produced at lower pressures, and thus variations in BND result from differences in nucleation. Some bubbles in all experiments appear to have been coalescing when quenched, especially at greater ΔP values. The measured BND values are thus minima.

Bubbles are attached to small and large magnetite crystals in all decompressions below 150 MPa (Fig. 1). BND values listed in Table 3 are for those nucleated on the small crystals. We note that the decompressions are considerably less than that required for homogenous bubble nucleation (Gardner and Ketcham, 2011; Hajimirza et al., 2021). We therefore assume that all bubbles nucleated on a crystal. In some cases, a crystal cannot be seen attached to a bubble, but because the crystals are so small it is likely that it is hidden from view.

Two suites of experiments were run at $\Delta P = 6$ and 13 MPa for quench times from 30 to 900 s (Table 3). At $\Delta P = 6$ MPa, the number of bubbles that nucleated on small crystals is nearly constant at $10^{7.1–7.6}$ cm^{-3} between 300 and 900 s. At $\Delta P = 13$ MPa, the number of bubbles nucleated on small crystals increase substantially between 30 and 150 s, but then remain constant at $\sim 10^{8}$ cm^{-3} to 450 s. These results indicate that bubbles nucleated relatively rapidly, and melt-bubble equilibrium was reached within ~300 s. For a BND = 10^{7} cm^{-3}, with an average bubble diameter of 6 μm, equally spaced bubbles are separated by ~40–50 μm. At 850 °C, H_2O could diffuse ~80 μm (twice the separation of bubbles) within 150 s in rhyolitic melt with ~4.5 wt% H_2O (Ni and Zhang, 2018). We thus conclude that bubble nucleation on the small magnetite microlites had ceased by ≤150 s.

Whenever bubbles nucleated on the small crystals there is only one bubble attached to a crystal (Fig. 1a). Bubbles are attached to ~10 % of the small crystals at $\Delta P = 6$ MPa, ~70 % of them at $\Delta P = 13$ MPa, and on all of them at $\Delta P \geq 43$ MPa. These bubbles are 2–27 μm in size, with most being ~6 μm, and differ little in size regardless of degree of supersaturation or time held at low pressure. The number of bubbles that nucleated on large magnetite crystals also increases with increasing ΔP, from 5 bubbles on each crystal at $\Delta P = 3$ MPa to >10 on each at >20 MPa (Table 3). Bubbles on large crystals range in size from 1 to 26 μm, although more than 90 % are 1–4 μm in diameter (Fig. 1b).

4. Discussion

Comparison of samples held isobarically at 6 or 13 MPa for various times shows that differences in BND between the runs resulted from the increase in ΔP of 7 MPa. Focusing on samples that quenched after 300 s shows that the increase in ΔP from 3 to 58 MPa generated more than two orders of magnitude increase in the number of bubbles nucleated on the small crystals, from $10^{6.4}$ to $10^{8.7}$ cm^{-3} (Fig. 2). That increase in BND is not, however, linear with ΔP, but instead most of the increase occurred between $\Delta P = 3$ and 23 MPa. At $\Delta P = 43–58$ MPa, BND is constant at $10^{8.7}$ cm^{-3} (Fig. 2). Over the same range in ΔP, the number of bubbles that nucleated on surfaces of large magnetite crystals increases (Table 3). These results suggest that the number of bubbles that can heterogeneously nucleate on crystals in a rhyolitic melt is controlled to a first order, by ΔP. But this is only valid up to a certain point. Our results also suggest that the number of bubbles that can nucleate is limited by the numbers of crystals available as nucleation sites.

The rate of heterogeneous bubble nucleation (J_{het}) can be modeled using a modified version of nucleation rate derived from classical nucleation theory (Hurwitz and Navon, 1994; Gardner et al., 2023):

$$J_{het} = \sum \beta_i J_i exp\left(\frac{-16\pi\sigma_{\infty}^{3}}{3k_B T(\Delta P)^2}\alpha_i\right) \quad (1)$$

where σ_∞ is the bulk surface tension in the melt, k_B is the Boltzman constant, T is temperature, and ΔP is supersaturation pressure. The α_i term is a correction factor that accounts for the reduced surface tension as a result of the presence of the heterogeneity. The pre-exponential term is the product of J_i, the nucleation rate in the absence of energy barriers, and β_i, the number density of heterogenous nucleation sites (Gardner et al., 2023). As written, J_{het} is the sum of rates on all heterogeneous sites (i) that exist. The cumulative number density of bubbles is given by the integration of Eq. (1) over the amount of time allowed for nucleation. As discussed, our results suggest that nucleation ceased within 150 s.

Examination of Eq. (1) shows that the J_{het} should increase as supersaturation increases, which to first order agrees with our results (Fig. 2). Holding all other variables constant, increasing ΔP from 3 to 58 MPa only increases J_{het} by ~11 %. It would thus not be expected that bubble number density increases two orders of magnitude (Fig. 2). In fact, most of the increase in bubble number density occurred as ΔP increased from 3 to 23 MPa (Fig. 2). We thus speculate that although ΔP is a major control on the final number density of bubbles, other factors must have impacted nucleation kinetics.

Heterogeneous nucleation can occur at relatively low ΔP values because the presence of pre-existing surfaces reduces the surface tension energy barrier to nucleation (Hurwitz and Navon, 1994). The α in Eq. (1) accounts for this lower energy and varies from 1 and 0, with $\alpha = 1$ representing homogeneous nucleation and $\alpha < 1$ accounting for nucleation on heterogeneities. The value of α comes from the geometric balance of surface tensions between the three phases, crystal (c), bubble (b), and melt (m) (Landau and Lifshitz, 1980; Hurwitz and Navon, 1994). For a spherical bubble partially wetting a flat crystal face α is given by

$$\alpha = \frac{1}{4}\left((2 - cos\theta)(1 + cos\theta)^2\right) \quad (2)$$

where θ is the contact angle between bubble and crystal and approximates the balance of surface tensions, such that

$$cos\theta = (\sigma_{cv} - \sigma_{cn})/\sigma_{mv} \quad (3)$$

where σ_{ij} is surface tension between two of the three phases (Landau and Lifshitz, 1980; Hurwitz and Navon, 1994). In lieu of being able to measure θ, α can be approximated from

$$\alpha \approx \left(\Delta P_{het}/\Delta P_{hom}\right)^2 \quad (4)$$

where ΔP_{het} is supersaturation needed to trigger heterogeneous nucleation and ΔP_{hom} is supersaturation needed for homogeneous nucleation

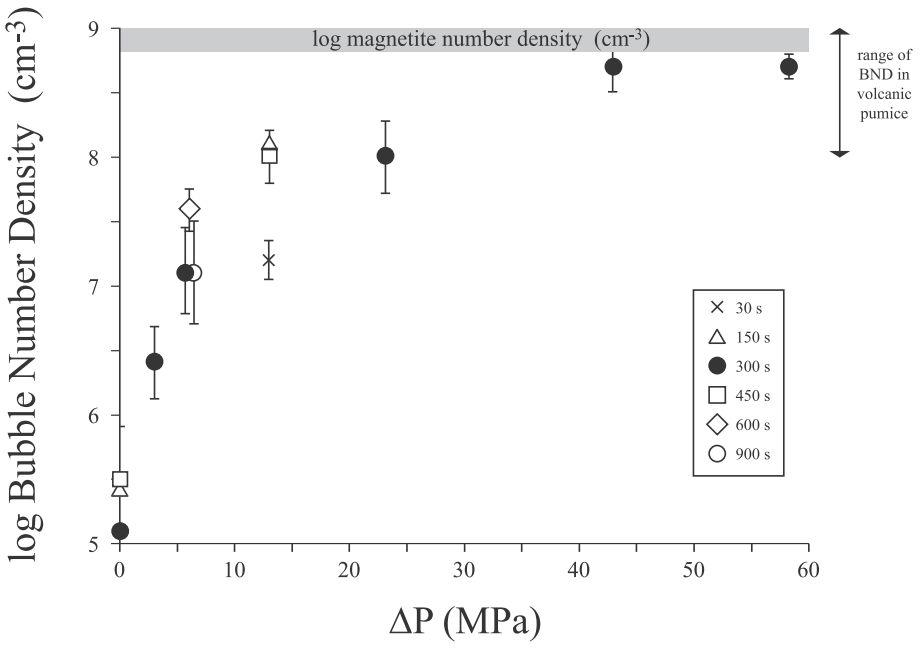

Fig. 2. Variation in BND with ΔP for small magnetite microlites. BND increases nearly four orders of magnitude between ΔP = 3 MPa–43 MPa. Symbols represent times held at low pressure. Error bars indicate BND standard deviations for each experiment. See Table 3 for data. The range in BND values for most explosively erupted volcanic pumice is shown, summarized from Cáceres et al., 2020.

(Gardner and Denis, 2004; Hajimirza et al., 2021; Gardner et al., 2023). The same rhyolitic melt used in this study had been used in numerous other experiments that focused on homogeneous bubble nucleation (Gardner et al., 2013; Hajimirza et al., 2019). Those experiments show that ΔP_{hom} is ~110–120 MPa for this melt with ~5 wt% H_2O. Here, we find that bubbles nucleated at ΔP_{het} = 3 MPa, and hence $\alpha \approx$ 0.0006–0.0007. Such a small value of α reduces the exponential in Eq. (1) to ≈ 1, and thus $J_{het} \approx \sum \beta_i J_i$, which would imply that all magnetite crystals should act as nucleation sites at low ΔP. This is contrary to our results, as it took ΔP > 23 MPa for bubbles to nucleate on all crystals (small and large) (Fig. 2).

It may be possible that σ_{ij} changes with increased ΔP (Eq. (3)). In classical nucleation theory, the interface between the bubble and the surrounding fluid is assumed to be sharp and well-defined, leading to a single value for σ_{mv} (Navon and Lyakhovsky, 1998; Lubetkin, 2003; Merikanto et al., 2007; Gonnermann and Gardner, 2013). Experimental results, however, are more consistent with a diffuse inhomogeneous boundary region around a bubble nucleus resulting in a gradient in surface tension between bubble and melt (Lubetkin, 2003; Gonnermann and Gardner, 2013; Hajimirza et al., 2019; Gardner et al., 2023). Tolman (1948) estimated the deviation of surface tension of bubbles depending on their size by using a characteristic thickness of the boundary region that has come to be called the Tolman length (δ_T). It may be possible that such a boundary region occurs at the melt–crystal interface and grows with increasing supersaturation, increasingly facilitating bubble nucleation on crystal faces as ΔP increases. We note, however, that σ_{mv} is unlikely to have been lowered significantly at the relatively small ΔP values of our decompressions, because homogeneous nucleation in this melt, which is controlled by σ_{mv}, occurs at ΔP = 110–120 MPa. Values for σ_{cm} and σ_{cv} are not known and so such an effect can only be speculated. If this were the main factor, however, it stands to reason that nucleation should occur on all crystals once a given ΔP is reached rather than gradually as ΔP increases (Fig. 2).

The numbers, sizes, and shapes of crystals are similar in all experiments, and so none of these could have changed with increasing ΔP to trigger greater nucleation. Although crystals do not differ between experiments, we note that bubbles nucleated on only ~10 % of available small magnetite and only a few bubbles nucleated on the large crystals at low ΔP values. At greater values of ΔP, however, bubbles nucleated on a greater proportion of small and large crystals until, at ΔP = 43 MPa, all small crystals had a bubble attached and the large crystals had multiple bubbles attached. Previous studies have found similar results. Both Hurwitz and Navon (1994) and Gardner and Denis (2004) found that few bubbles nucleated on magnetite at low ΔP, but multiple bubbles nucleated on single magnetite grains at greater ΔP. These observations suggest that different sites and different numbers of sites on crystals may have different activation energies. Greater amounts of ΔP might be required to overcome those various activation energies, which would explain why the number of bubbles nucleated depends on the relative amount of supersaturation. If so, this would imply that different values for α are associated with different sites on crystals, and thus Eq. (1) should be modified to account for not just different crystal types but also crystal "activation sites".

Finally, we found that more than one bubble can nucleate on relatively large crystals, with the number increasing with greater ΔP (Fig. 3). In fact, multiple bubbles have been observed on relatively large magnetite in volcanic pumice (Gualda and Anderson, 2007). The increased number with greater ΔP may again result from different sites becoming activated. In addition, we suggest that multiple bubbles can nucleate on large crystals because nuclei are far enough apart that diffusive loss of H_2O to one nucleus from the nearby melt does not impact melt supersaturation at other sites. Equating β in Eq. (1) to the CND of an entire crystal population is therefore not sufficient. Instead, as suggested by Gardner et al. (2023), the β term should be adjusted to account for multiple bubbles nucleating on larger magnetite crystals.

4.1. Implications

This study and that of Hurwitz and Navon (1994) found that bubbles can nucleate on magnetite at ΔP <5 MPa (Table 3). Such low ΔP values argue that $\alpha \approx 0$ in Eq. (1). Modeling studies have thus often assumed that bubbles nucleate on all available magnetite crystals at very low ΔP values (e.g. Hajimirza et al., 2021). Our results show that instead, BND is strongly controlled by ΔP and only reaches the number density of crystals when ΔP is relatively high (Fig. 2). Models for magma degassing thus need to parameterize α to account for the control of ΔP on

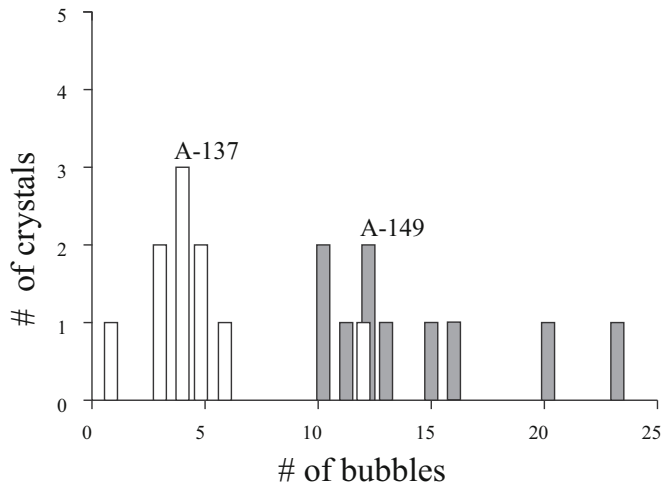

Fig. 3. Histogram showing the distributions of the number of bubbles nucleated on 10 large magnetite at dP = 3 MPa (A-137) and dP = 58 MPa (A-149). The x-axis shows the numbers of bubbles on any individual crystal. The y-axis shows how many crystals have the corresponding number of bubbles attached to them. A-137 = clear bars, A-149 = shaded bars.

nucleation kinetics.

At relatively high supersaturations, we find that a bubble nucleated on essentially every 1–2 μm sized magnetite, but there is no more than one bubble per crystal (Fig. 1a). This is likely because the crystals are small enough that diffusive loss of H_2O from the melt to the first nucleus lowers the local supersaturation around the crystal and prevents further nucleation. In this case, the end result is that BND equates to the number density of crystals, which can be written as

$$\int J_{het} dt = \sum \beta_i \tag{5}$$

where $\sum \beta_i$ is the summation of all crystals that serve as nucleation sites for one bubble.

Recent studies have argued that nanolites (crystals <1 μm) are the main facilitators for heterogeneous bubble nucleation (Shea, 2017; Cáceres et al., 2020; Brachfeld et al., 2024; McCartney et al., 2024). Given our results, it seems unlikely that such small crystals can nucleate more than one bubble each. This implies that the number density of bubbles in explosively erupted pumice approximates the minimum number density of nanolites present when bubbles nucleated. The BND values of pumice in explosive eruptions range from 10^7 to 10^{11} cm^{-3}, with more than 80 % of the data falling within the range of 10^8–10^9 cm^{-3} (Cáceres et al., 2020). The minimum number density of nanolites in most magmas that erupt explosively would thus have to exceed ~10^7 cm^{-3}, if all bubbles nucleated on nanolites.

Despite there being ~10^9 cm^{-3} small magnetite crystals in our samples, ΔP had to exceed 23 MPa for bubbles to nucleate on essentially all crystals. Interestingly, the resulting BND values overlap with the majority of those measured in explosively erupted pumice (Fig. 2). Studies of nanolites in explosively erupted magmas have found nanolite number densities as high as 10^{16} cm^{-3} (e.g. Mujin and Nakamura, 2014; Mujin et al., 2017; Cáceres et al., 2020). If magmas have nanolite populations up to ~10^{16} cm^{-3}, then it is feasible that most bubbles in pumice could have nucleated at small ΔP. Alternatively, our results could imply that magmas become relatively highly supersaturated before they erupt explosively.

5. Conclusions

Our results demonstrate that the number of bubbles that can nucleate on magnetite crystals in a rhyolitic melt is controlled to first order by the amount of supersaturation (ΔP), until all available nucleation sites have been occupied. Once those sites are utilized, greater supersaturation does not result in additional heterogeneous bubble nucleation. The number of sites available, however, appears to be related to the degree of ΔP. At small degrees of ΔP some sites are activated, and a few bubbles can heterogeneously nucleate on magnetite. Only at relatively high degrees of ΔP can bubbles nucleate on all available small crystals and numerous bubbles can nucleate on large crystals. To allow modeling of heterogeneous bubble nucleation to account for these findings, we propose that the α term in the nucleation rate Eq. (1) should be a variable that differs for different nucleation sites available. In addition, the pre-exponential term β_i in Eq. (1) should account for different size fractions of crystals (Gardner et al., 2023). Bubble number densities generated in our experiments are within the same order of magnitude of those in most natural pumice samples. This implies that either the number densities of nanolite crystals in magmas greatly exceeds $10^{8–9}$ cm^{-3}, or explosively erupted rhyolitic magmas supersaturate by ≥20 MPa in order for bubbles to nucleate in the numbers seen.

CRediT authorship contribution statement

Wade L. Aubin: Writing – review & editing, Writing – original draft, Investigation, Formal analysis, Data curation, Conceptualization. **James E. Gardner:** Writing – review & editing, Writing – original draft, Funding acquisition, Formal analysis, Conceptualization.

Declaration of competing interest

The authors declare that they have no known competing financial interests or personal relationships that could have appeared to influence the work reported in this paper.

Acknowledgements

JEG and WLA were supported by the National Science Foundation under NSF GEO-NERC Award Number: 2211627, "Collaborative Research: A general model for bubble nucleation and growth in volcanic systems." Suggestions from two anonymous reviewers significantly improved this manuscript.

Appendix A. Supplementary data

Supplementary data to this article can be found online at https://doi.org/10.1016/j.jvolgeores.2024.108218.

Data availability

Data will be made available on request.

References

Brachfeld, S., McCartney, K.N., Hammer, J.E., Shea, T., Giachetti, T., 2024. Evaluating the role of titanomagnetite in bubble nucleation: rock magnetic detection and characterization of nanolites and ultra-nanolites in rhyolite pumice and obsidian from Glass Mountain, California. Geochem. Geophys. Geosyst. 25, e2023GC011336.
Cáceres, F., Wadsworth, F.B., Scheu, B., Colombier, M., Madonna, C., Cimarelli, C., Hess, K.-U., Kaliwoda, M., Ruthensteiner, B., Dingwell, D.B., 2020. Can nanolites enhance eruption explosivity? Geology 48, 997–1001.
Cáceres, F., Scheu, B., Colombier, M., Hess, K.-U., Feisel, Y., Ruthensteiner, B., Dingwell, D.B., 2022. The roles of microlites and phenocrysts during degassing of silicic magma. Earth Planet. Sci. Lett. 577, 117264.
Cichy, S.B., Botcharnikov, R.E., Holtz, F., Behrens, H., 2011. Vesiculation and microlite crystallization induced by decompression: a case study of the 1991–1995 Mt Unzen eruption (Japan). J. Petrol. 52, 1469–1492.
Cluzel, N., Laporte, D., Provost, A., Kannewischer, I., 2008. Kinetics of heterogeneous bubble nucleation in rhyolitic melts: implications for the number density of bubbles in volcanic conduits and for pumice textures. Contrib. Mineral. Petrol. 156, 745–763.
Fiege, A., Holtz, F., Cichy, S.B., 2014. Bubble formation during decompression of andesitic melts. Am. Mineral. 99, 1052–1062.

Gardner, J.E., 2007. Bubble coalescence in rhyolitic melts during decompression from high pressure. J. Volcanol. Geotherm. Res. 166, 161–176.
Gardner, J.E., 2009. The impact of pre-existing gas on the ascent of explosively erupted magma. Bull. Volcanol. 71, 835–844.
Gardner, J.E., 2012. Surface tension and bubble nucleation in phonolite magmas. Geochim. Cosmochim. Acta 76, 93–102.
Gardner, J.E., Denis, M.-H., 2004. Heterogeneous bubble nucleation on Fe-Ti oxide crystals in high-silica rhyolitic melts. Geochem. Cosmochem. Acta 68, 3587–3597.
Gardner, J.E., Ketcham, R.A., 2011. Bubble nucleation in rhyolite and dacite melts: temperature dependence of surface tension. Contrib. Mineral. Petrol. 162, 929–943.
Gardner, J.E., Webster, J.D., 2016. The impact of dissolved CO2 on bubble nucleation in water-poor rhyolite melts. Chem. Geol. 420, 180–185.
Gardner, J.E., Hilton, M., Carroll, M.R., 1999. Experimental constraints on degassing of magma: isothermal bubble growth during continuous decompression from high pressure. Earth Planet. Sci. Lett. 168, 201–218.
Gardner, J.E., Ketcham, R.A., Moore, G., 2013. Surface tension of hydrous silicate melts: constraints on the impact of melt composition. J. Volcanol. Geotherm. Res. 267, 68–74.
Gardner, J.E., Hajimirza, S., Webster, J.D., Gonnermann, H.M., 2018a. The impact of dissolved fluorine on bubble nucleation in hydrous rhyolite melts. Geochim. Cosmochim. Acta 226, 174–181.
Gardner, J., Wadsworth, F., Llewellin, E., Watkins, J., Coumans, J., 2018b. Experimental sintering of ash at conduit conditions and implications for the longevity of tuffisites. Bull. Volcanol. 80, 23.
Gardner, J., Wadsworth, F., Llewellin, E., Watkins, J., Coumans, J., 2019. Experimental constraints on the textures and origin of obsidian pyroclasts. Bull. Volcanol. 81, 22.
Gardner, J.E., Wadsworth, F.B., Carley, T.L., Llewellin, E.W., Kusumaatmaja, H., Sahagian, D., 2023. Annu. Rev. Earth Planet. Sci. 51, 131–154.
Girona, T., Costa, F., Schubert, G., 2016. Degassing during quiescence as a trigger of magma ascent and volcanic eruptions. Sci. Rep. 5, 18212.
Gonnermann, H.M., Gardner, J.E., 2013. Homogeneous bubble nucleation in rhyolitic melt: experiments and nonclassical theory. Geochem. Geophys. Geosyst. 14, 11.
Gualda, G.A.R., Anderson, A.T., 2007. Magnetite scavenging and the buoyancy of bubbles in magmas. Part 1: Discovery of a pre-eruptive bubble in Bishop rhyolite. Contrib. Mineral. Petrol. 153, 733–743.
Hajimirza, S., Gonnermann, H.M., Gardner, J.E., Giachetti, T., 2019. Predicting Homogeneous Bubble Nucleation in Rhyolite. J. Geophys. Res. Solid Earth 124, 2395–2416.
Hajimirza, S., Gonnermann, H.M., Gardner, J.E., 2021. Reconciling bubble nucleation in explosive eruptions with geospeedometers. Nature Comm. 12, 283.
Hamada, M., Laporte, D., Cluzel, N., 2010. Simulating bubble number density of rhyolitic pumices from Plinian eruptions: constraints from fast decompression experiments. Bull. Volcanol. 3, 735–746.
Hirth, J.P., Pound, G.M., Pierre, G.R.S., 1970. Bubble nucleation. Metal. Trans. 1, 939–945.
Hurwitz, S., Navon, O., 1994. Bubble nucleation in rhyolitic melts: experiments at high pressure, temperature, and water content. Earth Planet. Sci. Lett. 122, 267–280.
Iacono-Marziano, G., Schmidt, B.C., Dolfi, D., 2007. Equilibrium and disequilibrium degassing of a phonolitic melt (Vesuvius AD 79 “white pumice”) simulated by decompression experiments. J. Volcanol. Geotherm. Res. 161, 151–164.
Iacono-Marziano, G., Morizet, Y., Trong, E., Gaillard, F., 2012. New experimental data and semi-empirical parameterization of H_2O-CO_2 solubility in mafic melts. Geochim. Cosmochim. Acta 97, 1–23.
Iacovino, K., Moore, G., Roggensack, K., Oppenheimer, C., Kyle, P., 2013. H_2O-CO_2 solubility in mafic alkaline magma: applications to volatile sources and degassing behavior at Erebus volcano, Antarctica. Contrib. Mineral. Petrol. 166, 845–860.
Landau, L.D., Lifshitz, E.M., 1980. Statistical Physics. Pergamon, New York.
Larsen, J.F., 2008. Heterogeneous bubble nucleation and disequilibrium H_2O exsolution in Vesuvius K-phonolite melts. J. Volcanol. Geotherm. Res. 175, 278–288.
Le Gall, N., Pichavant, M., 2016. Homogeneous bubble nucleation in H_2O- and H_2O-CO_2-bearing basaltic melts: results of high temperature decompression experiments. J. Volcanol. Geotherm. Res. 327, 604–621.
Liu, Y., Zhang, Y., Behrens, H., 2005. Solubility of H_2O in rhyolitic melts at low pressures and a new empirical model for mixed H_2O–CO_2 solubility in rhyolitic melts. J. Volcanol. Geotherm. Res. 143, 219–235.
Lubetkin, S.D., 2003. Why is it much easier to nucleate gas bubbles than theory predicts? Langmuir 19, 2575–2587.
Mangan, M.T., Sisson, T.W., 2000. Delayed, disequilibrium degassing in rhyolite magma: decompression experiments and implications for explosive volcanism. Earth Planet. Sci. Lett. 183, 441–455.
Mangan, M.T., Sisson, T.W., Hankins, W.B., 2004. Decompression experiments identify kinetic controls on explosive silicic eruptions. Geophys. Res. Lett. 31, L08605.
McCartney, K.N., Hammer, J.E., Shea, T., Brachfeld, S., Giachetti, T., 2024. Evaluating the role of titanomagnetite in bubble nucleation: Novel applications of low temperature magnetic analysis and textural characterization of rhyolite pumice and obsidian from Glass Mountain, California. Geochem. Geophys. Geosyst. 25, e2023GC011338.
Merikanto, J., Zapadinsky, E., Lauri, A., Vehkamaki, H., 2007. Origin of the failure of classical nucleation theory: incorrect description of the smallest clusters. Phys. Rev. Lett. 98, 145702.
Mourtada-Bonnefoi, C.C., Laporte, D., 1999. Experimental study of homogeneous bubble nucleation in rhyolitic magmas. Geophys. Res. Lett. 26, 3505–3508.
Mujin, M., Nakamura, M., 2014. A nanolite record of eruption style transition. Geology 42, 611–614.
Mujin, M., Nakamura, M., Miyake, A., 2017. Eruption style and crystal size distributions: Crystallization of groundmass nanolites in the 2011 Shinmoedake eruption. Am. Mineral. 102, 2367–2380.
Navon, O., Lyakhovsky, V., 1998. Vesiculation processes in silicic magmas. Geol. Soc. Lond. Spec. Publ. 145, 27–50.
Ni, H., Zhang, L., 2018. A general model of water diffusivity in calc-alkaline silicate melts and glasses. Chem. Geol. 478, 60–68.
Proussevitch, A.A., Sahagian, D.L., 1996. Dynamics of coupled diffusive and decompressive bubble growth in magmatic systems. J. Geophys. Res. 101 (B8), 17447–17455.
Proussevitch, A.A., Sahagian, D.L., 1998. Dynamics and energetics of bubble growth in magmas: Analytical formulation and numerical modeling. J. Geophys. Res. 103, 18223–18251.
Proussevitch, A.A., Sahagian, D., 2005. Bubbledrive-1: a numerical model of volcanic eruption mechanisms driven by disequilibrium magma degassing. J. Volcanol. Geotherm. Res. 143, 89–111.
Sahagian, D.L., 2005. Volcanic eruption mechanisms: Insights from intercomparison of models of conduit processes. J. Volcanol. Geotherm. Res. 143, 1–15.
Shea, T., 2017. Bubble nucleation in magmas: a dominantly heterogenous process? J. Volcanol. Geotherm. Res. 343, 155–170.
Sparks, R.S.J., 1978. The dynamics of bubble formation and growth in magmas: a review and analysis. J. Volcanol. Geotherm. Res. 3, 1–37.
Tolman, R.C., 1948. Consideration of the Gibbs theory of surface tension. J. Chem. Phys. 16, 758–774.
Tramontano, S., Gualda, G.A.R., Ghiorso, M.S., 2017. Internal triggering of volcanic eruptions: tracking overpressure regimes for giant magma bodies. Earth Planet. Sci. Lett. 472, 142–151.